Spin-wave modes in Ni nanorod arrays studied by Brillouin light scattering

A. A. Stashkevich, Y. Roussigné, P. Djemia, and S. M. Chérif
LPMTM CNRS (UPR 9001), Université Paris 13, 93430 Villetaneuse, France

P. R. Evans, A. P. Murphy, W. R. Hendren, R. Atkinson, R. J. Pollard, and A. V. Zayats
Centre for Nanostructured Media, Queen's University of Belfast, Belfast BT7 1NN, United Kingdom

G. Chaboussant and F. Ott
Laboratoire Léon Brillouin CEA/CNRS, CEA Saclay, 91191 Gif sur Yvette Cedex, France
(Received 5 April 2009; revised manuscript received 23 June 2009; published 12 October 2009)

Dynamic magnetic properties of arrays of Ni nanorods with a low aspect ratio have been investigated. It has been shown that the spectra of spin-wave resonances localized on nanorods with a low aspect ratio typically feature the presence of zones with high density of states resulting in a characteristic two-peak pattern of Stokes and anti-Stokes lines of magneto-optical (MO) Brillouin light scattering with pronounced Stokes–anti-Stokes (S-AS) asymmetry. A simple theoretical model based on the analysis of the elliptic character of the polarization of the optical wave interacting with a dipole magnetostatic wave has been proposed. It has been shown that the S-AS asymmetry is due entirely to the asymmetry of the MO interaction efficiency with respect to time reversal of the magnetic precession in a magnon.

DOI: 10.1103/PhysRevB.80.144406 PACS number(s): 75.30.Ds, 75.50.−y, 78.35.+c

I. INTRODUCTION

Magnetic properties of electrodeposited arrays of metal (Co, Ni, and Permalloy) nanowires in a dielectric substrate have been intensively studied during the last decade both theoretically and experimentally (see Ref. 1 and references therein). Nanowires have been shown to exhibit magnetoresistance,[2] giant magnetoresistance (GMR),[3–5] and support coherent spin waves.[6] Potential applications in data storage devices have stimulated interest in magnetization reversal in individual wires,[7,8] including current-induced magnetization switching (CIMS).[9] Other potential applications of arrays of magnetic nanowires are in microwave devices. One of the attractive features of such structures, owing to their geometry, is the possibility of synthesizing materials with a desirable value of uniaxial magnetic anisotropy oriented along the wire axis. Previous experimental ferromagnetic resonance (FMR) studies[10–12] relying mainly on the strip-line technique have allowed measurement of microwave absorption in nanowires excited by a homogeneous external electromagnetic field in a wide frequency range. Using a planar microstrip transmission line,[13–16] dipolar interactions in electrodeposited Ni nanowire arrays were characterized as a function of the packing density P (4–38%) and the wire diameter (56–250 nm) for typical nanowire length of tens of microns (aspect ratio over 50). The dipolar interactions between the wires were modeled, according to a mean-field approach assuming an effective uniaxial anisotropy field oriented perpendicular to the wire axis and proportional to the membrane porosity.

In a broader context, magnetic nanorod and nanowire structures fall into a broad category of nanocomposite ferromagnetic metamaterials whose properties, including dynamic behavior in the microwave frequencies, can be tailor made for a specific application. Other noteworthy structures within this class of artificial materials are based on films comprised of ferromagnetic nanospheres in a nonmagnetic matrix.[17,18] Typically, the size of the magnetic particles is small (on the order of several nanometers), which makes applicable the theoretical methods based on the simplified "superspin" model.[19,20] Here each nanoparticle is associated with a "magnetic point" having no internal structure giving a relatively simple and clear physical picture. In particular, the transition from superparamagnetism (SPM) (Ref. 19) to superferromagnetism (SFM) (Ref. 20) via the superspin glass[19] state has been implemented by simply varying the particle concentration. The main physical principle, underlying the static and dynamic magnetic behavior of nanocomposite materials is a formation of collective propagating modes from individual oscillations initially localized on individual nanoelements. Scenarios of such transition from individual to collective behavior vary considerably depending on the geometry of nanoelements. In the widely used Damon-Eshbach configuration, in which magnetization is in the plane of the substrate and electromagnetic wave propagates along the surface perpendicular to magnetic field, these modes can be the *exchangeless* surface Damon-Eshbach (DE) magnetostatic waves (MSWs) governed by dipole-dipole interactions (DDIs) and spin-wave resonance (SWR) modes, whose behavior is determined by the exchange interaction.

Early theoretical papers[21,22] on magnetic excitations in cylindrical geometry treated them as purely magnetostatic modes. However, recent theoretical descriptions of dynamic properties of arrays of nanowires have also taken into account the dipole-exchange nature of the magnetization waves in nanowires. Their behavior has been thoroughly investigated by Arias and Mills who have developed a powerful analytic technique both for dipole-exchange modes localized in individual cylindrical wires[23] and collective modes in arrays of such wires.[24] At the same time, their analysis was limited to the particular case of purely cylindrical geometry when the external magnetic field and static magnetization are parallel to the wire axis. A more general situation, with an arbitrary orientation of the magnetization with respect to the

axis of symmetry, was analytically treated by Tartakovskaya.[25]

It should be noted that all previous experimental research was carried out on "quasi-infinite" nanowires with the aspect ratio R typically ranging from 20 to 100. In theory this favors simplified analytical approaches based on the "quasi-infinite" solution along the "z" axis. Consequently, vertical spin-wave resonances were not taken into account and theoretical interpretation relied fully on the azimuthal modes. Interestingly, to fit experimentally measured frequency separation between azimuthal modes of the order of several GHz on a 30 nm nanowire it was necessary to diminish by one order of magnitude, the value of the exchange constant with respect to its bulk value.[25]

In this paper we study the dynamic properties of arrays of Ni nanorods with aspect ratios $R=9$ and $R=2.5$ so that vertical spin-wave resonances, previously neglected in the studies of nanowires with $R>50$, become extremely important. In both samples the Ni nanorods were 175 nm long, while their diameter was equal to 20 and 70 nm, respectively. With the packing density P being in the intermediate range of values (12.5% and 15.5%), both individual and collective aspects of spin-wave behavior were to be taken into account.

For the observation of magnetic modes, Brillouin light scattering (BLS) was used. BLS was successfully employed previously for characterizing thermal magnons localized on various nanostructures, such as patterned ferromagnetic multilayers,[26–28] arrays of long Ni nanowires,[29,30] Co nanospheres in a SiO_2 matrix,[31,32] and arrays of Ni nanorings.[33] A multiscale modeling has been adopted to achieve theoretical description of the observed effects since a fully rigorous analysis is hardly realistic in view of the complexity of the structure studied. We relied on purely numerical techniques for the analysis of individual magnetic behavior of nanorods, while simplified analytic expressions based on effective magnetic and optical parameters were obtained to take account of the collective features in the dynamic behavior of the system. The near-field nature of optical interactions in the nanorod arrays was also taken into account.

II. SAMPLE PREPARATION AND EXPERIMENTAL TECHNIQUE

A. Sample fabrication

To fabricate a template for nanorod electrodeposition, Al films were grown on buffer layers of gold and tantalum on silicon substrates by rf magnetron sputter deposition. The tantalum was necessary as an adhesion layer to avoid delamination on anodization of the aluminum and the gold layer allows good electrodeposition into the pores.[34] Anodization and hence pore formation were carried out at constant voltage using a platinum counter electrode. The size and spacing of the pores is found to be linearly dependent on the anodization voltage. For this work the aluminum was anodized at 20 V in 0.3 M sulphuric acid which produced 20-nm-diameter pores with ~40 nm spacing and at 40 V in 0.3 M oxalic acid to produce 70-nm-diameter pores with ~90 nm spacing. The electrolyte was cooled below 275 K and the temperature monitored throughout the process. After a brief etch to remove the barrier layer at the bottom of the pores, nickel rods were grown by potentiostatic electrodeposition from a 0.1 M $NiSO_4$ solution at a voltage of −1 V versus a saturated calomel electrode. Both samples were grown for 60 s to produce rods of ~175 nm as estimated from electron microscope images (Figs. 1 and 2). These images of the arrays of the nickel rods deposited in the 20 nm (sample A) and 70 nm (sample B) pores, respectively, also show that the filling fraction of the pores is high in both cases and is close to 100% for the 20 nm pores.

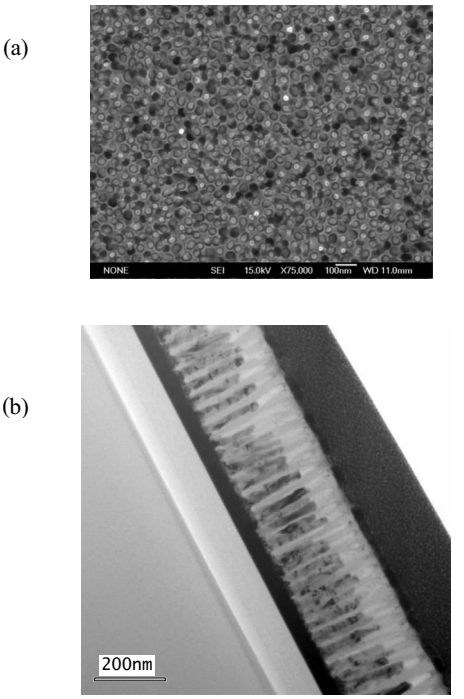

FIG. 1. (a) SEM image of Ni nanorods grown in 20 nm pores. The alumina matrix has been briefly etched to expose the rods. (b) TEM cross section of 20 nm Ni rods.

B. Neutron scattering

In order to check overall characteristics of the samples, neutron reflectivity was performed at the Laboratoire Léon Brillouin (LLB) laboratory with a neutron wavelength $\lambda = 8$ Å. The sample was rotated, and the reflected neutrons were collected in a two-dimensional (2D) X-Y detector of 128×128 pixels (64×64 cm) situated at a distance $D_0 = 4$ m from the sample position. The data obtained on the two samples are shown in Fig. 3. The schematic of the experiment is shown as inset.

Specular reflectivity is sensitive to the in-depth atomic composition profile of the surface. The refractive index of a simple surface is given by the product of the atomic density ρ and the nuclear neutron scattering length b:

$$n = 1 - \frac{\lambda^2}{2\pi}\rho b.$$

The critical angle θ_c of total reflection is given, as in classical optics, by

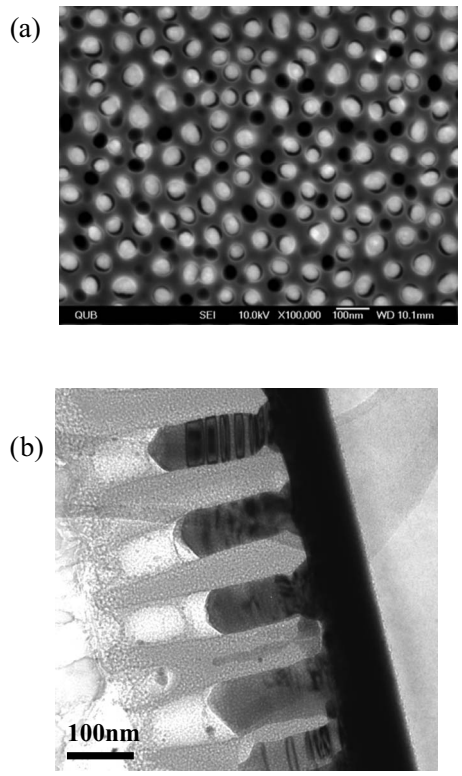

FIG. 2. (a) SEM image of Ni nanorods grown in 70 nm pores, the aluminum oxide has been briefly etched to expose the rods. It can be seen that the filling ratio is lower than for the 20 nm pores. (b) TEM cross section of 70 nm Ni rods.

$$\sin(\theta_c) = \sqrt{\frac{\rho b}{\pi}}\lambda.$$

In a multilayer, these expressions are more complicated and we resort to a model taking into account the atomic composition and densities of the various layers. During fitting, all the parameters of the inner layers (thickness, density, and composition) are kept fixed according to the sample parameters derived form SEM images (Figs. 1 and 2). To avoid

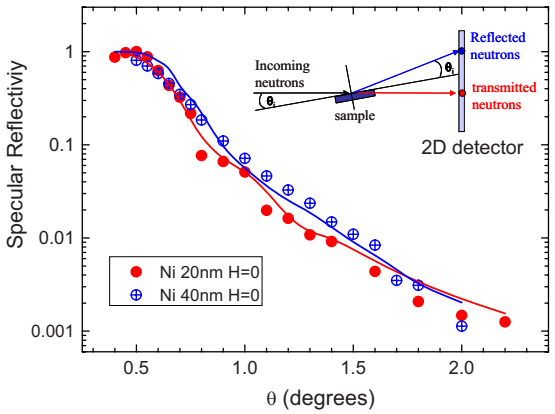

FIG. 3. (Color online) Neutron specular reflectivity of Ni 20 nm and Ni 70 nm obtained on the spectrometer PAPYRUS at LLB-Saclay (CEA-CNRS) with a neutron wavelength $\lambda = 8$ Å. The angle θ is the incident angle.

"overparameterization," the neutron-scattering length parameters b are also kept fixed according to the porosity of the arrays and the ratio of Ni to Al_2O_3 in the sample. The thickness and the density of the Al_2O_3/Ni layer are floating parameters. The results of the fits are shown in Fig. 3. A good overall agreement is found with a critical angle $\theta_c = 0.5°$ so that $\langle \rho b \rangle = 37.3 \times 10^{-6}$ nm^{-2}. We find that a good description of the reflectivity profile is achieved by considering total nanoporous layer thickness of 160 nm for sample A and 370 nm for sample B. This is good agreement for the 20 nm rod sample but gives an overestimate of the length of the 70 nm rods. It should be noted that the thickness evaluation severely depends on the porosity and the exact content of the pores. The obtained atomic densities are in agreement with a 12.5% and 15.5% pore concentration inferred from scanning electron microscopy (SEM) data.

C. Brillouin scattering

The BLS measurements in the *p-s* polarization configuration were carried out in the Damon-Eshbach geometry: the bias magnetic $\vec{H}$ (0.0–10 kOe) field was applied parallel to the plane of the film and the direction of the in-plane wave vector characterizing the investigated magnetic excitation was normal to $\vec{H}$. Light from a single-mode Ar^+ laser of 350 mW power at wavelength $\lambda = 514$ nm was focused onto the sample and the frequency spectrum of the backscattered light was analyzed using a computer controlled Sandercock-type (2×3)-pass tandem Fabry-Pérot interferometer. The wave number K was changed by varying the angle of light incidence θ measured with respect to the surface normal of the sample from 0° to 65°:

$$K = (4\pi/\lambda)\sin\theta.$$

Cross polarizations between the incident and scattered beams were used in order to practically suppress the light scattered by phonons. The acquisition time in BLS measurements was on the order of 1 h which compares favorably with 8 h reported in Ref. 30.

III. RESULTS AND DISCUSSION

A. Magneto-optical properties

Studies of magnetic hysteresis were carried out by sensing the magneto-optical Kerr effect (MOKE), using a photoelectric modulator based instrument,[35] at 633 nm. The hysteresis loops are shown in Fig. 4 and were measured in two configurations: the Longitudinal configuration, where the applied magnetic field was in the plane of the sample and perpendicular to the rods; the polar configuration, where the applied magnetic field was perpendicular to the plane of the sample and along the axis of the rods.

In both configurations, the loops showed significant remanence and coercivity although the latter was particularly high for the polar measurements. In the longitudinal configuration, the 20 nm nanorods had higher remanence and were more easily magnetized than the 70 nm nanorods, and in the polar configuration, the 20 nm rods had lower remanence and were less easily magnetized than the 70 nm rods.

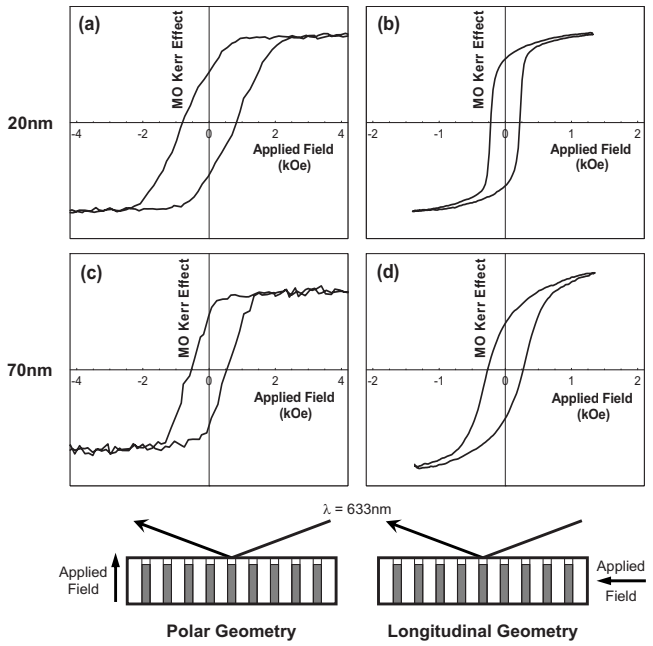

FIG. 4. The polar and longitudinal MOKE hysteresis loops for 20 and 70 nm diameter Ni rods measured at a wavelength of 633 nm. The loops are as follows: (a) polar loop for 20 nm nanorods; (b) longitudinal loop for 20 nm nanorods; (c) polar loop for 70 nm nanorods; (d) longitudinal loop for 70 nm nanorods. Schematics of the polar and longitudinal configurations are also shown.

The magnetic behavior of the samples in the polar geometry can be explained in terms of conventional reasoning. Within the "macrospin" model, the coercive field in this configuration is determined entirely by the anisotropy of the sample. Since there is little difference in the packing density of the samples, the major factor relevant to this discussion is the aspect ratio. Sample A is characterized with a higher $R=9.0$, which corresponds to a high "initial" value of the anisotropy in an isolated wire and less pronounced inter-rod interactions with respect to the case $R=2.5$. Numerical estimations performed according to the method reported in Ref. 36 based on the macrospin approach, return the following values of the demagnetizing factor: $I_{xx}=(2\pi)\times 0.86$ for sample A and $I_{xx}=(2\pi)\times 0.78$ for sample B, thus confirming the tendency following from the qualitative considerations. It is also corroborated by the experimental curves in Figs. 4(a)–4(c). However, there is a considerable quantitative discrepancy between the approximate theoretical approach and the experiment, pointing to the inadequacy of the macrospin concept in the investigated samples especially in the case when the cylinders are not saturated. More specifically, it emphasizes the importance of the inhomogeneity of the static magnetization including the presence of the domain structure. This discrepancy becomes even more pronounced in the longitudinal geometry, where the remanence and the coercitivity are entirely due to the above-mentioned inhomogeneity. The analytical formalisms developed so far although flexible and computer friendly rely entirely on the simplistic "even magnetization" approximation and thus must be fully excluded from being applied to the geometry studied. That is why in our theoretical analysis *a rigorous numerical approach*, however time consuming, is employed. Taking into account the complex inhomogeneous nature of the distribution of the magnetization in a nanorod, in the static as well as in the dynamic calculations, it ensures reliable and adequate theoretical description.

B. Brillouin scattering

As is well known, for zero external magnetic field $H=0$ the magnetization inside an individual rod of infinite length is parallel to its axis owing to the shape anisotropy. This is also the case for our finite cylinders. For an infinite cylinder the effective field of perpendicular uniaxial shape anisotropy H_a is equal to $2\pi M_s$. To take account of the inter-rod dipolar interactions the authors of Ref. 15 have introduced effective anisotropy $H_a^{dip}=H_a-6\pi PM_s$, where P is the packing density of nanorods. Thus for $P=0$, H_a^{dip} is equal to its value in an individual rod and for $P=1$ to its value for a continuous film. Introduction of effective parameters describing simultaneously both types of anisotropy, as has been shown in Refs. 15 and 16 is justified in the case of purely magnetostatic modes in quasi-infinite ($R>10$) nanorods. It is not evident, however, that it works even for purely magnetostatic modes in the case of rods of finite height. Lateral and transverse sizes being comparable, all three sets of exchange modes: azimuthal, radial, and vertical should be taken into account. That is why for the theoretical analysis we have chosen a numerical technique based on a finite-element approach[37] that can fully describe the dynamic response of individual nanorods. For comparison, we also consider analytically described modes in spheroidal particles (the Kittel modes) replacing a cylinder by a prolate spheroid (long semiaxes $a=88$ nm along Oz, small semiaxes $b=c=10$ or 35 nm along Ox and Oy axes) with the applied external field along the Ox direction. Its frequency is given for the nonsaturated case $H<(N_x-N_z)4\pi M_s$ by

$$\omega=\gamma\sqrt{[(N_z-N_x)4\pi M_s]^2-H^2} \tag{1}$$

and for the saturated case $H>(N_x-N_z)4\pi M_s$

$$\omega=\gamma\sqrt{H[H+(N_z-N_x)4\pi M_s]}, \tag{2}$$

where γ is the gyromagnetic factor and N_x, N_y, N_z are the demagnetizing factors[38] of a prolate spheroid.

Preliminary theoretical analysis based on the bulk value of the exchange constant shows that in an array of nanorods 175 nm high the mode frequency separation due to the vertical (along z axis) quantization of the spin-wave number can exceed several GHz and needs to be taken into account. These modes will be referred to subsequently as vertical SWRs. Naturally, the frequencies of the azimuthal and radial resonances localized on the cylinders of diameter of 20 and 70 nm are higher. It should be noted that the expected cross section of BLS scattering from vertical SWR modes must be greater than that from the azimuthal modes.

Two sets of BLS measurements, both in the Damon-Eshbach geometry, have been performed. We started with the dependence of the modal frequency on the intensity of the magnetic field applied in the plane of the film and normal therefore to the rod axis.

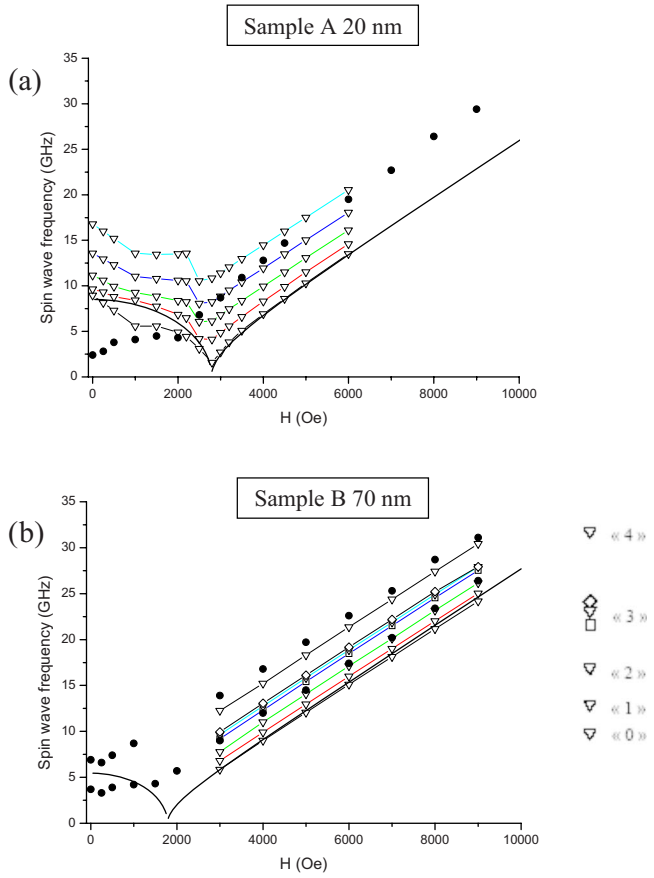

FIG. 5. (Color online) The dependence of the theoretical (empty symbols) and experimental values (filled circles) of resonance frequencies as a function of the intensity of magnetic field applied normally to the axis of a rod for the sample (a) $D=20$ nm and (b) $D=70$ nm. Also shown is the calculated Kittel mode for an ellipsoid with a 175-nm-long axis and the value of the rod diameter taken as a small axis (line).

The dependence of the theoretical (empty symbols) and experimental (filled circles) values of resonance frequencies as a function of the intensity of the magnetic field applied perpendicular to the axis of a rod are given in Fig. 5 for both samples. The nature of the SWR resonances involved as well as the symbols employed will be discussed later, in the context of the Fig. 7, illustrating the identification of SWRs.

The angle of incidence of light was 45°. The following numerical values were taken for the magnetic parameters of Ni: $4\pi M_s=6000$ G, $g=2.18$ and exchange constant $A=8\times10^{-7}$ erg/cm. The numerical analysis made by the finite-element method includes the contribution of the exchange and the intrarod dipole interaction but not the inter-rod coupling. In other words, actual resonances on individual rods are considered. Also shown is the calculated frequency of the Kittel mode for an ellipsoid with a 175-nm-long axis and the value of the diameter taken as small axis (solid line). Experimental peaks are marked with solid circles. Theoretical frequencies are represented by empty symbols. Even in a smaller 20 nm rod array the theoretical spectra in a nonsaturated sample are so dense and irregular that one can hardly trace the evolution of the frequency of a given mode with the increasing magnetic field [Fig. 5(a)]. In the bigger 70 nm one it is practically impossible [Fig. 5(b)]. On the contrary, if the films are saturated the modes excited at a given frequency are easily identifiable. Interestingly, in both cases, the numerically estimated frequency of the lowest mode agrees fairly well with the Kittel mode frequency determined analytically with the corresponding ellipsoid geometry (prolate spheroid) especially in a saturated sample. This coincidence is closer for the rods with a higher aspect ratio, i.e., in the case of $D=20$ nm. Apparently, for the 70 nm rods, the relation between the geometric parameters of a cylinder and an equivalent ellipsoid is less straightforward.

As is predicted by an approximate magnetostatic theory the frequency of the lowest resonance turns to zero when $H=H_a^{dip}$. The shape anisotropy of an individual infinite rod is equal to $H_a=2\pi M_s=3000$ G, while the overall anisotropy, taking into account the inter-rod dipole interaction for the sample $D=70$ nm with a packing density $P=0.15$ amounts to $H_a^{dip}=1650$ Oe. The value of H corresponding to the zero frequency H_0 obtained via theoretical estimations, both numerical and analytical, of eigenfrequencies in an individual cylinder with a small aspect ratio $R=2.5$, is of the order of 1800 Oe, which is rather close to 1650 Oe. In other words, in this particular geometry the influence of inter-rod dipole interactions and the influence of a finite aspect ratio of an individual rod R on the effective value of magnetic anisotropy H_0 are similar. Both factors diminish the magnetic anisotropy. For the sample with a higher aspect ratio this difference is more pronounced: $H_a^{dip}=1875$ Oe and $H_0=2400$ Oe.

Typical BLS spectra in fully saturated samples for the angle of incidence $\theta=45°$ are given in Fig. 6(a) (the sample with $D=70$ nm saturated with an external magnetic field $H=7000$ Oe) and Fig. 6(b) (the sample with $D=20$ nm saturated with an external magnetic field $H=5000$ Oe). While in the 20 nm sample only one peak is observed, at least two separate peaks can be resolved in the case of 70 nm rods with the exception of two points in the vicinity of $H=2000$ Oe. This value corresponds to the transition from out of plane to the in-plane magnetization orientation, in which case the resonance frequencies drop considerably. For this reason only peak has been observed in the BLS spectra. The width of each peak as well as the overall width of the double spectral line in Fig. 6(a) is indicated with arrows. These data are represented in Fig. 5(b) with vertical error bars. To avoid overcharging of Fig. 5(b), we have plotted this information only for one value of the saturating magnetic field, namely, $H=7000$ Oe. For other external fields no appreciable variations of the width of the spectral lines has been observed. Interestingly, while there is a pronounced Stokes–anti-Stokes (S-AS) asymmetry in the spectra obtained on 70 nm nanorods, in the case of the 20 nm nanorods the Stokes–anti-Stokes bands are only slightly asymmetric.

To identify the modes appearing in Figs. 5 and 6 we calculated the profiles of the first five lowest in frequency resonances. To classify resonances we ascribe three indices to each mode: n for vertical resonances along the axis of each rod (z axis), m for azimuthal (angular) modes, and l for radial modes. In the case of thin 20 nm cylinders with a high value of the aspect ratio ($R=9$) results are easily predictable: all

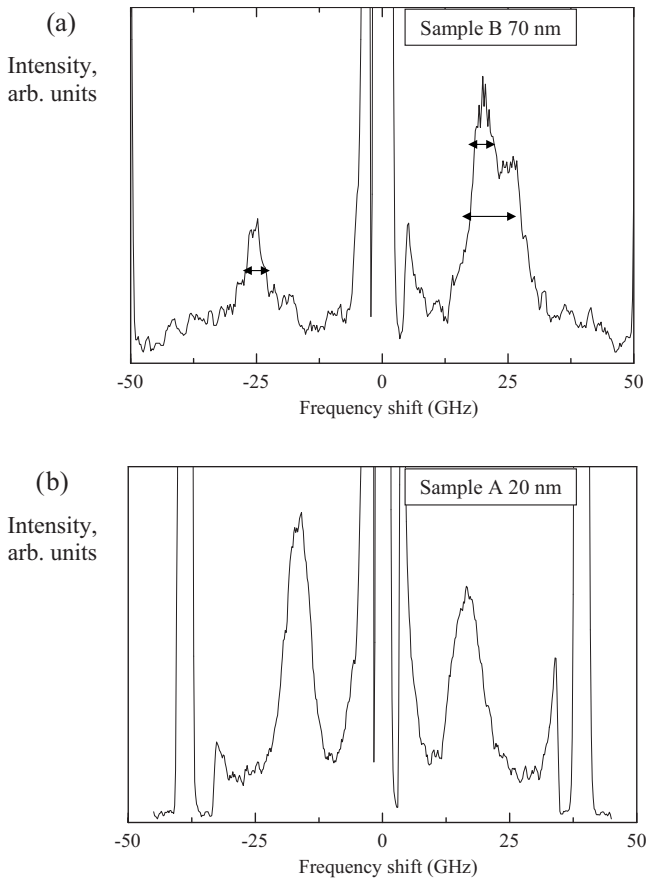

FIG. 6. Typical BLS spectra in a fully saturated samples for angle of incidence $\theta=45°$ for the case (a) $D=70$ nm, $H=7000$ Oe and (b) $D=20$ nm, $H=5000$ Oe.

five modes are vertical, i.e., resonances along the z axis. For obvious reasons the first azimuthal and radial modes ($m=1$, $l=0$ and $m=0$, $l=1$) will appear only at the frequencies in the vicinity of vertical resonances with $n \approx R=9$.

Identification of the modes in thick rods required far more considerable theoretical effort. Their azimuthoradial as well as vertical profiles for the 70 nm sample are presented in Fig. 7. The value of the external magnetic field was taken equal to $H=3000$ Oe, which is sufficient to saturate the sample. The code used in the numerical simulations based on the dissipation-fluctuation theorem and finite element approach returns the distributions of the square of the dynamic magnetization (the z component) of thermal magnons on the axis of a nanocylinder. It is clearly seen that along the vertical axis z these functions are periodic or quasiperiodic and can be classified, as in the previous case, according to the number of nulls: $n=0,1,2,\ldots$. Although, strictly speaking, not purely sinusoidal along z, their shapes are close to that in an infinite continuous film. For this reason, a reasonable rough estimation of the resonance frequencies can be made from the formulas for a continuous film using the effective parameter approach.

However, the behavior of the modes in the vicinity of the top and bottom surface of a finite cylinder is not trivial. It resembles the distribution of purely magnetostatic modes localized on an infinite stripe magnetized along its axis inves-

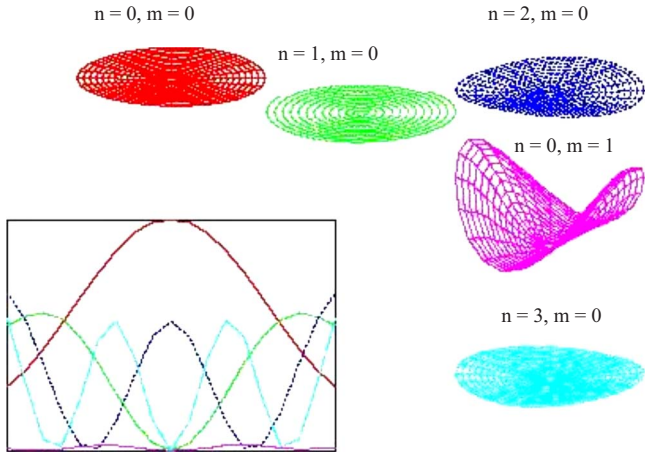

FIG. 7. (Color online) Profiles of dynamic magnetization localized on a nanocylinder of height $h=175$ nm and with a diameter $D=70$ nm and (aspect ratio equal to 2.5) with the saturating magnetic field $H=3000$ Oe.

tigated analytically[39,40] and numerically.[41] These distributions can be described in terms of the useful notion of "dipolar pinning" introduced in Ref. 39. Although in our numerical simulations the spins were taken to be free at the top and bottom surfaces of a nanocylinder in neither case, like in a purely magnetostatic approximation,[39–41] the derivative of the magnetization with respect to z tends to zero at $z=0$, h (here h is the height of a cylinder). This can be explained by an appreciable contribution of dipolar interactions within each cylinder. Nonzero "dipolar" pinning is most pronounced in the fundamental mode $n=0$ where the role of demagnetizing field at the edges is most significant. One of the consequences of these edge effects is the fact that the corresponding wave number characterizing the standing wave resonances is no longer described by a simplified relation $k=n\pi/h$. According to Ref. 41, n should be replaced by $n-1/3$ to take into account dipolar demagnetizing in an infinite stripe. It is not certain, however, that such a simple correction is sufficient in the case of nanocylinders. A similar tendency to nonzero pinning at the edges can be seen in the rigorous theoretical analysis of dipole modes on nanostripes carried out in Ref. 39. Clearly, by appropriately decreasing the meshing step of the numerical procedure one could arrive at vanishing of the derivative with respect to z in the very vicinity of each edge, thus explicitly revealing the "free spin" boundary conditions assumed for numerical simulations. However, the overall tendency to dipolar pinning emphasizes the role of magnetostatic interactions and inadequacy, in the case considered, of the Aharoni approximation taking into account only exchange coupling in the analysis of submicron particles.[42]

The distribution in the "$r\varphi$" plane, normal to the axis of the cylinder for these first three modes, is uniform. In other words, these are purely vertical SWRs with $n=0$, 1, and 2. Such standing modes are denoted with triangles with its sequential number "n" indicated nearby: "0," "1," and "2" (see Fig. 5). Next comes the first azimuthal mode $m=1$ with a uniform vertical $n=0$ distribution. It should be mentioned that, strictly speaking, its radial distribution is not absolutely

uniform, just as in the case of the classic Bessel function solution. However, this inhomogeneity can be barely seen (Fig. 7, cross section $n=0$, $m=1$). Correspondingly, its frequency does not fall into the same category as the series of the first three vertical modes and is designated with a square. The next resonance is again purely vertical: $n=3$, $m=0$, and $l=0$, indicated, as previously, by a triangle with its ordinal number "3." Further calculations show that it is followed a mode of the radial type $n=0$, $m=0$, and $l=1$. It is indicated by a lozenge. Interestingly, for the given value of the aspect ratio $R=2.5$ the latter three modes are closely spaced in the frequency domain, thus forming a "cluster" of three consecutive resonances. In other words, the simulations have revealed two points of high density of states in the SWR spectra. To facilitate the interpretation of the symbols in Fig. 5, a special inset in Fig. 5(b) has been added. It is a large-scale reproduction of the SWR spectrum for a given value of the magnetic field ($H=6000$ Oe). As it has been mentioned above, to distinguish the nature of resonances, the following symbols are used for each type of mode: open triangles for vertical resonances, open squares for azimuthal resonances and open lozenges for radial ones.

We have not succeeded in resolving the optical response of each single SWR mode, which is not surprising: the samples are not homogeneous enough. This concerns mainly the height of individual nanorods, which leads to broadening of the BLS lines. At the same time, the BLS resolution is sufficient to reveal the two distinctive peaks related to the two points of spectral concentration of SWR resonances localized on nanorods. This double-peak BLS fine structure is the characteristic signature of the investigated sample configuration. The first subpeak, as usual, corresponds to the fundamental Kittel mode and its nearest neighbor. Typically, in all planar ferromagnetic structures their magnetooptical contribution is most significant. In our case, however, the MO interaction takes place in the near-field regime and the character of the overlapping of the interacting optical field and high-frequency magnetization is not at all trivial especially since the optical skin effect is also to be taken into account. This important point will be dealt with in detail in the last section of this paper, focusing on the role of the MO mechanisms involved. As for the second sub-peak, it is engendered by a cluster of vertical, azimuthal, and radial modes in the vicinity of the $n=3$ mode. The later feature is due to the specific value of the aspect ratio $R=2.5$.

As it has been mentioned above, in the 20 nm sample all the frequencies appearing in Fig. 5(a) correspond to modes of vertical type with $n=0$, 1, 2, 3, and 4. Thus no points with high density of states can possibly appear in the SWR spectrum. Moreover, the contribution of the fundamental Kittel mode is preponderant in the optical BLS response. The explanation lies in the near-field nature of the MO interaction within the sample, which manifests itself in two ways. First, the optical field penetrates the nano-size sample from all sides in more or less symmetric way, there is no "shadow" side for a nanoelement. Second, due to the fact that the diameter of 20 nm is smaller than the optical skin depth, the distribution of the optical field within a nanorod is relatively even. This means that the overlap integral of the interacting optical and magnetic fields, characterizing the MO efficiency, is considerably reduced for higher SWRs ($n>1$), especially for antisymmetric odd modes. Thus the absence of the points of concentration of the density of states in the SWR spectra together with a relative suppression due to symmetry considerations, of the responses of higher SWRs invariably lead to a single-peak BLS line in the thin 20 nm sample.

It is well known that a perfectly homogeneous distribution of the static magnetization in a saturated state can be reached only in the samples of ellipsoidal form. In a cylinder of a finite aspect ratio, which is not strictly speaking an ellipsoid, there are zones, in the vicinity of the sample edges, of highly uneven static magnetization. They can be regarded as tiny resonance cavities with highly localized SW modes confined within each such zone. This effect has been discovered in arrays of micrometric stripes of by the authors of the Refs. 43 and 44. Interestingly, they used a conventional BLS setup without additional microfocusing. Although such cavities, also known as "quantum wells," are small, still in the case of scattering by micrometric stripes, the conventional far-field diffraction mechanisms are predominant. For obvious reasons an extremely wide angle scattering from these objects has been observed: the signal was completely smeared in the inverse "K" space. In our case of nanosize three-dimensional (3D) magnetic scattering elements the localization of the "wells" is far more pronounced. Moreover these tiny nanozones produce a purely near-field diffraction pattern. In other words, the expected cross section of such scattering is insignificant and, not surprisingly, we have not detected the optical response of the quantum well modes.

One of major points addressed in this paper is the mechanism underlying dynamic magnetic properties of a nanocomposite material. More specifically, we focused on the role of the long-range dipole-dipole interactions between individual nanoelements comprising a nanocomposite planar structure in the collective dynamic behavior of the structure as a whole. The most significant features of the latter manifest themselves via collective modes propagating in the bulk of such structures. In other words, we seek to establish the relation between the effective parameters governing the behavior of the above-mentioned collective modes and the geometry of the nanostructure. In order to clarify this, the dispersion $\omega(K)$ of SWR modes was measured for different values of the applied magnetic field. The BLS spectra for different values of θ, i.e., for different values of K, are shown for sample B for $H=8000$ Oe in Fig. 8. For such a high value of the applied magnetic field the sample is fully saturated as indicated in Fig. 5. For normal incidence $\theta=0$ [Fig. 8(a)] the BLS spectrum, i.e., Stokes and anti-Stokes components, is almost perfectly symmetric. There are two pairs of peaks at a relatively low frequency of approximately 23 GHz (marked with arrows) and another one at a relatively high frequency of 28 GHz. Their origin, as explained above, is due to two points of concentration of resonance frequencies characteristic for the specific aspect ratio value of the sample. With the increase in θ the position of both peaks fluctuates around its mean value and do not show any observable dispersion. At the same time their amplitude changes drastically. First, low frequency peaks demonstrate a striking S-AS asymmetry even for a relatively small angle of

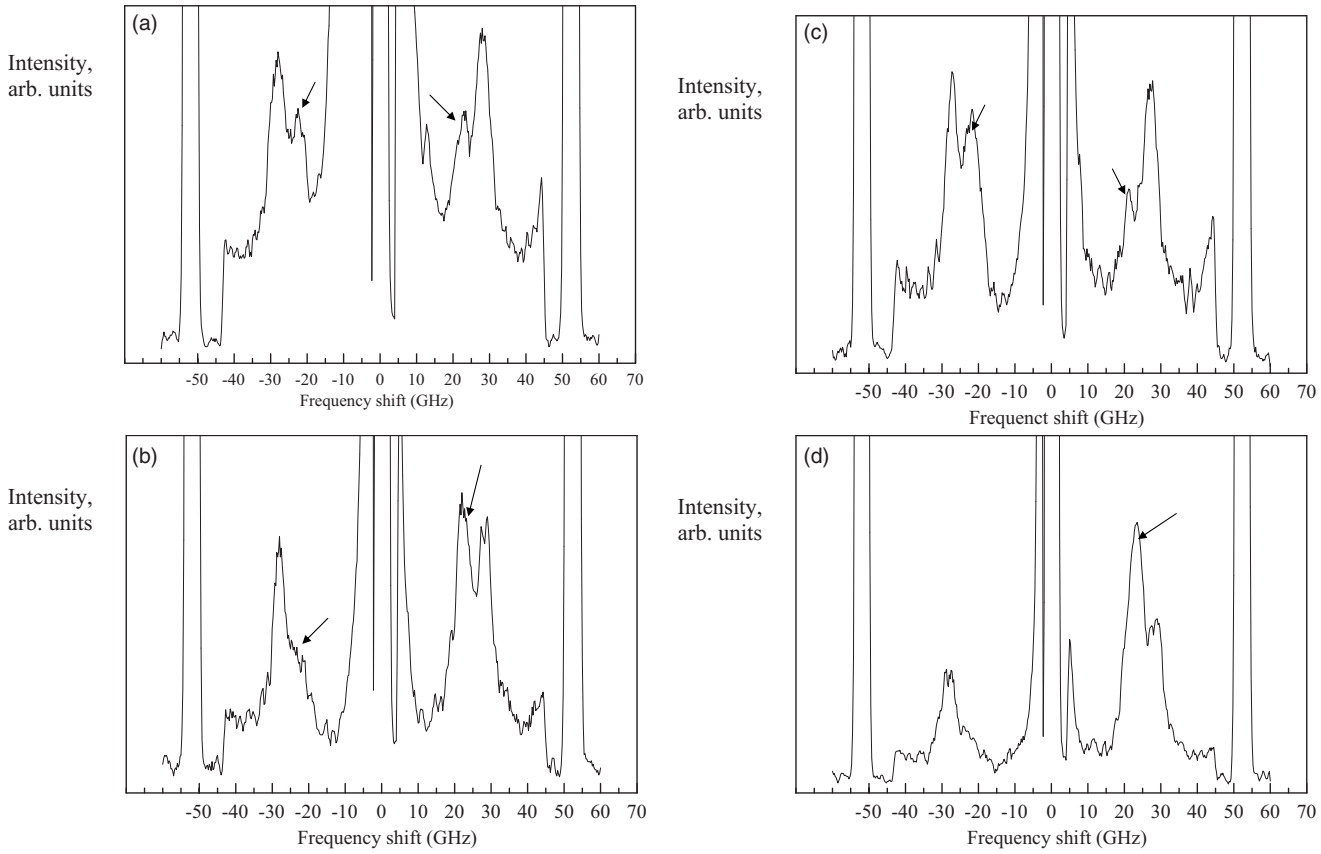

FIG. 8. BLS spectra measured in the sample with $D=70$ nm saturated with in-plane magnetic field $H=8000$ Oe in the Damon-Eshbach geometry (a) $\theta=0°$, (b) $\theta=15°$, (c) $\theta=-15°$, and (d) $\theta=55°$.

incidence $\theta=15°$ [Fig. 8(b)]. In a continuous film such asymmetry is a characteristic signature of a surface MSW mode (DE mode) confined to one of the film surfaces. Its wavelength is greater than the period of the array. In line with Damon-Eshbach behavior when $\theta=-15°$ [Fig. 8(c)], the asymmetry is inverted. For $\theta=55°$ [Fig. 8(d)] the anti-Stokes low-frequency peak dominates the spectrum: the amplitude of symmetric high-frequency maxima is at least two times smaller and the low-frequency anti-Stokes response practically disappears.

Interestingly, a similar two-peak structure of BLS spectra, including S-AS asymmetry, has been observed on nanocomposite films comprised of Co 4 nm grains imbedded in a SiO_2 matrix in the superferromagnetic (SFM) state[31] where symmetric high-frequency peaks are attributed to SWR nonpropagating resonances, while S-AS asymmetry is a distinctive signature of the Damon-Eshbach mode. In our case, however, the geometry of the nanocomposite medium is different: it is an assembly of relatively big nanorods characterized by a pronounced shape anisotropy whose spacing excludes direct exchange coupling. At the same time, the fundamental physical mechanisms leading to the formation of the purely dipole Damon-Eshbach mode, characterized by a pronounced dispersion, are identical. In both cases it is due to long-range dipole-dipole interactions (DDIs) coupling the fundamental (Kittel) modes ($n=0$, $m=0$, $l=0$) of purely dipole nature, localized on individual nanorods or nanospheres. In this respect, the system studied, in the saturated state, is close to a superparamagnetic state: its high-frequency dynamics is determined entirely by DDIs between nanoelements with a quasihomogeneous distribution of dynamic magnetization.[32] The analogy between the two systems however ends here. Higher exchange modes are created according to entirely different scenarios. While in dense SFM nanogranular films they are formed due to strong *interparticle* exchange interactions, in arrays of nano-rods studied in this work these are SWR due entirely to the *intraparticle* exchange stiffness, that are very weakly coupled though long-range DDIs.

In order to model the properties of the DE mode in nanorod arrays, the approximate mean field theory of the ferromagnetic resonance in arrays of magnetic rods proposed in Ref. 15 and outlined above was extended to the case of magnetostatic waves propagating in such structures with nonzero wave number K. In line with the effective medium mean field approach, applied to nanocomposite ferromagnetic films, we have supposed the effective magnetic anisotropy and the effective saturation magnetization to be equal to

$$H_a^{eff} = 2\pi M_s(N_z - N_x)(1-P), \tag{3a}$$

$$4\pi M_s^{eff} = 4\pi P M_s. \tag{3b}$$

In Eq. (3) P is a packing density of nanorods. To test validity of this approach we used the simple analytic formula derived in Ref. 45 for the Daman-Eshbach mode propagating in a

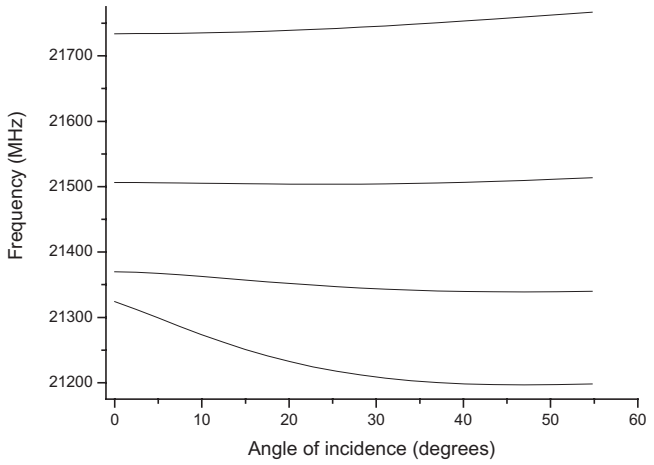

FIG. 9. Dispersion curves for the Damon-Eshbach mode and the first three spin-wave resonances.

magnetically anisotropic film for relatively low values of wave numbers $Kh \ll 1$. Here h is the film thickness. For the particular case of purely uniaxial magnetic anisotropy it can be further simplified

$$\omega = \sqrt{\omega_H[\omega_H + (\omega_M^{eff} - \omega_a^{eff})]} + \frac{\omega_M^{eff}(\omega_M^{eff} - \omega_a^{eff})}{\sqrt{\omega_H[\omega_H + (\omega_M^{eff} - \omega_a^{eff})]}} \frac{Kh}{4}. \tag{4}$$

Here $\omega_H = \gamma H$, $\omega_M^{eff} = \gamma 4\pi M_s^{eff}$, and $\omega_a^{eff} = \gamma H_a^{eff}$. According to Eq. (4) the group velocity of the DE mode in an anisotropic film is determined by $v_{gr} = \omega_M^{eff}(\omega_M^{eff} - \omega_a^{eff})/\sqrt{\omega_H[\omega_H + (\omega_M^{eff} - \omega_a^{eff})]}h/4$. In other words the dispersion changes sign when the effective anisotropy exceeds the effective saturation magnetization. Let us consider two limiting cases: a continuous monolayer ($P=1$) and an individual isolated rod ($P=0$). In the first case $\omega_M^{eff} = \omega_M$ and $\omega_a^{eff} = 0$ which leads to the classic dispersion formula for the DE mode. The notion of wave number loses sense for an individual rod, i.e., $K=0$. Besides, in this case $\omega_M^{eff} = 0$ and $\omega_a^{eff} = 2\pi M_s$, which brings us back to Eq. (2). For an infinite isolated cylinder this gives the classic formula for the ferromagnetic resonance $\omega = \gamma\sqrt{H(H - 2\pi M_s)}$.

Having defined effective parameters, we were able to estimate DE dispersion in our nanocomposite films making use of the tensor magnetic Green's-function approach. The results obtained for the 70 nm nanorods are given in Fig. 9. The order of the matrix reduction[46] was set equal to 3. It is clearly seen that the frequency range of approximately 100 MHz is largely insufficient to ensure detection of the dispersion by the BLS technique. Not surprisingly, numerical results obtained for the second 20 nm sample confirm the same conclusion. This explains why we have not succeeded in detecting the DE dispersion. In other words, although the inter-rod dipole interactions are non-negligible, clearly manifesting themselves in the static behavior (see the earlier discussion), they are, at the same time, not sufficiently strong to be noticeable in the dynamics.

Thus, relatively low concentration of magnetic nanoelements excludes direct detection of dispersion in the composite structure studied. However, as it has been shown in Refs. 31 and 32, the fine structure of the BLS spectra, especially the asymmetry in the amplitude of the Stokes and anti-Stokes components, can be very helpful in identifying the physical nature of magnetic excitations in nano-composite films. While exchange dominated non-propagating SWRs are characterized by a symmetric S-AS pattern, the purely dipole DE mode has a distinctive asymmetric signature. It should be noted that it is known for a long time, having been discovered as early as the late seventies.[47] At this early stage it was ascribed to the asymmetry of the spatial distribution of the DE mode with respect to the inversion of the magnetic field $\vec{H}$: if in the first case it is localized near the top of the ferromagnetic layer, in the second one its localization shifts to the bottom of the layer. Shortly afterwards, the subject was treated in full detail in Refs. 48 and 49, where the most general formalism based on the fluctuation-dissipation theorem (FDT) and optical Green's functions for a multilayer has been developed. Thus both the thermal stochastic nature of the magnons and macroscopic well defined magneto-optical properties of the structure were simultaneously taken into account. Computer simulations carried out have confirmed the presence of the S-AS asymmetry. Moreover, the subject was especially addressed in Ref. 50 which focused on the role of the nondiagonal spin-spin correlation functions $\langle S_x S_y \rangle$. This formalism, rigorous and sophisticated, was based on the earlier papers[48,49] and took into account multiple nontrivial aspects of the BLS in a planar structure, including their stochastic nature. Not surprisingly, no simple analytic expressions could have been derived. In the context of the present paper, considering a system of very complex geometry it is unjustifiably complicated. Sacrificing the generality, we propose an alternative approach focusing on the symmetry of the MO interaction. Being perfectly straightforward, it can be formulated in terms of a single surprisingly simple expression [see Eq. (A1)], thus providing more physical insight, lacking in the papers on the early 1980s. Moreover, it is compatible with the purely numeric COMSOL simulations (see the discussion below), which has allowed us to estimate, to the first approximation, the degree of the S-AS asymmetry.

Thus, in view of the complexity of the system studied, a fully rigorous analysis is hardly realistic that is why a multiscale approach has been adopted by us. We were seeking a compromise theoretical description approaching the real situation from the two natural limiting cases, namely, a quasi-continuous monolayer characterized by effective physical (magnetic and optic) parameters and an assembly of individual isolated nanorods. Thus, simple and efficient numerical procedures can be developed backed by simple and clear analytical expressions. Moreover, being mutually complementary, they ensure a comprehensive and adequate physical picture of the major features of the investigated effects.

In order to further clarify the important issue of the influence of the polarizations of the interacting waves: the incident optical wave, the scattered optical wave and the MSW, a very simple *ad hoc* analytical relation for the S-AS asymmetry has been obtained in the Appendix. The calculation is based on the purely classical approach, which makes it straightforward and its result physically clear: the S-AS

asymmetry reflects the fact that the mixed product $(\vec{e}_{(i)} \cdot (\vec{e}_{(s)} \times \vec{m}))$ is not symmetric with respect to the complex conjugation of one of two complex vectors ($\vec{e}_{(i)}$ and $\vec{m}$) appearing in it. The latter reflects the symmetry of MO effects in metals described by the antisymmetrical unitary Levi-Civita tensor. Actually, the latter statement can be reformulated in a surprisingly simple way which amounts to the following. In the case of scattering in *p-s* polarization configuration, the Stokes and anti-Stokes efficiency is proportional to the scalar product formed by two complex 2D polarization vectors. These are the polarization of the incident "*p*" wave (with its components permuted) and that of the polarization of the MSW in the anti-Stokes case (scattering by a magnon with a positive frequency $+\omega$) or its complex conjugate in the Stokes case (scattering by a magnon with a negative frequency $-\omega$). This complex conjugation is due to the fact that the inversion of the sign of the frequency of a magnon is equivalent to the time reversal of the magnetic precession in a magnon. In other words, the S-AS asymmetry is engendered entirely by the asymmetry of the MO interaction efficiency with respect to the time reversal of the magnetic precession.

To investigate the behavior of the polarization of the light scattered in the nanorod array, rigorous numerical finite element modeling was used (COMSOL MULTIPHYSICS package[51]). The nanorod array was assumed to have a square lattice, corresponding to the packing density of about 15%. The evolution in time, during a full period, of the electric field vector $\vec{E}_{(i)}$ components of the incident *p*-polarized optical wave inside a 70×175 nm nanorod was followed in the simulations for the optical wavelength used in the experiment $\lambda = 514$ nm (Fig. 10).

The top inset illustrates the configuration of the points 1–7. To make the graphs more clear for understanding and to avoid complicated designations, the horizontal time axis is normalized to a full period, thus the abscissa varies from 0 to 2π. Moreover, such format of presentation of the results allows direct reading of the phase shift between the components of the electric field, which is necessary for the estimation of the S-AS asymmetry. The angle of incidence was set equal to the values used in the experiment: 0°, 15°, and 55°.

As expected, the field in the middle of the rod is attenuated due to a small skin depth of Ni which is on the order of 30 nm. The near-field nature of electromagnetic diffraction by nanorods results in the situation that amplitudes in symmetric points on opposite sides of the rods are practically equal (points 3 and 7). At the same time, the simulations have revealed several interesting features. First, polarization is almost linear in all the points lying on the center line (2, 4, and 6), especially in point 4 that is the center of symmetry of a nanorod. In contrast, there is a non-negligible ellipticity in the polarization of $\vec{E}_{(i)}$ on the surface of the rod (1, 3, and 5), being especially pronounced in point 3. Interestingly, even in the case of normal incidence, there are zones where the ellipticity is nonzero in particular in points 3 and 7 that are situated symmetrically with respect to the center-line of the rod. However, as can be seen in Fig. 10, the sign of the phase mismatch in point 3 is reversed with respect to that in point 7. This polarization behavior explains the presence of S-AS

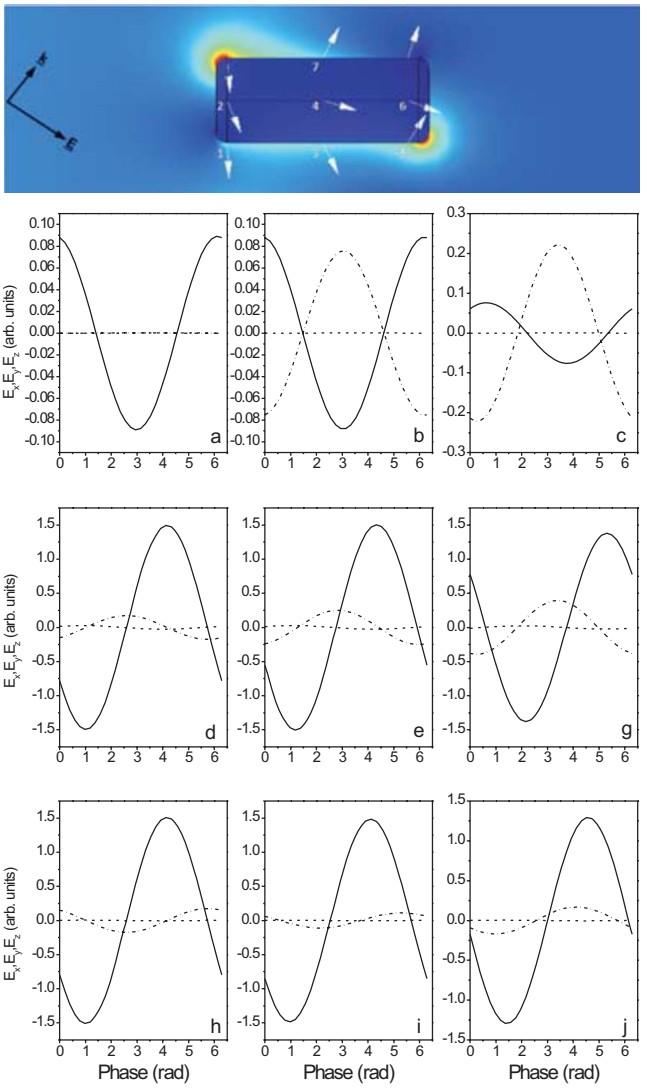

FIG. 10. (Color online) Numerical simulations of the distribution of the electric field components within a nanorod in points 3, 4, and 7 for different angles of incidence (0°, 15°, and 55°). The evolution in time, during a full period, of all the components of the electric field vector $\vec{E}_{(i)}$ of the incident *p*-polarized optical wave inside a 70×175 nm nanorod. The inset on top illustrates the geometry of the points 1–7.

asymmetry in the Brillouin scattering spectra. There are two characteristic zones within each nanorod where the light polarization is strongly elliptic: these are symmetric points 3 and 7. Besides, the direction of the rotation of the $\vec{E}_{(i)}$ vector in these points is opposite, which means that the zones engender two S-AS patterns with opposite asymmetry. In the case $\theta = 0°$, for obvious reasons, the distribution of the $\vec{E}_{(i)}$ field is identical in both zones which means that the two contributions to the optical response are equal and their superposition finally produces an entirely symmetric S-AS pattern. With the increase in θ the contribution of the zone 3 becomes preponderant.

To numerically estimate the plausibility of this hypothesis, we calculated the ratio $I^{anti\text{-}Stokes}/I^{Stokes}$ (see the Appendix), taking into account the field polarization around the

nanorods. To this end, the actual values of light polarization were extracted form numerical simulations (Fig. 10), while the ellipticity of the magnetic mode was taken equal to that of the Kittel mode.[52] This simple theoretical model predicts the increase in the S-AS asymmetry with the growth of θ. Moreover, for the specific experimental values of $\theta=15°$ and $\theta=55°$, $I^{anti\text{-}Stokes}/I^{Stokes}=1.6$ and $I^{anti\text{-}Stokes}/I^{Stokes}=2.4$, which correspond well to the experimental values.

IV. CONCLUSION

The BLS spectra from nanorods with a low value of the aspect ratio are characterized by two major features, namely, a two-peak structure of BLS lines and a high degree of S-AS asymmetry. The former is explained by the presence of zones with high density of states in the spectrum of the SWR modes localized on a nanorod, each producing a separate subpeak. To estimate the SWR spectra and to identify the modes, we used a purely numerical finite element technique which returns also the distribution of the dynamic magnetization. These numerical simulations have revealed nonnegligible dipole pinning on the top and on the bottom of a rod. The effect is the most pronounced for the purely dipole Kittel mode.

No SW dispersion has been detected which is explained, within a simple mean-field theory, by too low packing density. The S-AS asymmetry, typically ascribed to collective behavior of the DE type, here is due entirely to the elliptic character of the polarization of the light interacting with magnetostatic waves. Moreover, it is a direct consequence of the asymmetry of the MO interaction efficiency with respect to the time reversal of the magnetic precession in a magnon.

Numerical simulations of the light polarization within a nanorod led to a simple theoretical model providing a qualitative and partially quantitative description of this effect.

ACKNOWLEDGMENTS

This work was supported by the French Ministry of National Education and Research (ACI NR0095 "NANODYNE") and EPSRC-GB (UK). We would like to thank P. Moch and M. Kostylev for helpful discussions. We would also like to thank E. Tartakovskaya for the help in the numerical estimation of the demagnetizing factors.

APPENDIX

Typically, in the BLS experiment a plane optical wave, backscattered by a SW mode in the metallic film, is created by a plane-wave incident on the air-metal interface under an angle θ. For the sake of simplicity, let us consider the case of a semi-infinite metal slab. Since optical attenuation in metallic media is significant, its index of refraction has a pronounced imaginary component $n+i\kappa$ and consequently $\varepsilon=\varepsilon_1+i\varepsilon_2=(n^2-\kappa^2)+i2n\kappa$. Thus the components of the wave vector $\vec{k}=k_x\vec{u}_x+k_z\vec{u}_z$ are given by the following complex expressions:[53]

$$k_x = k_0 \sin\theta, \quad k_z = k_0(q+ip),$$

where

$$q=[(\varepsilon_1-\sin^2\theta)^2+(\varepsilon_2)^2]^{1/4}\cos(\varphi/2),$$

$$p=[(\varepsilon_1-\sin^2\theta)^2+(\varepsilon_2)^2]^{1/4}\sin(\varphi/2),$$

with

$$\varphi=\arctan\left(\frac{\varepsilon_2}{\varepsilon_1-\sin^2\theta}\right).$$

There are two major factors that determine the efficiency of a three-wave MO interaction. The first one is the overlap integral which quantifies the spatial correlation of distributions of the fields of three interacting waves within the interaction volume. Henceforth we will refer to it as the *spatial factor*. The second one is a factor which quantifies the "correlation" of the polarizations of the three waves referred as the *vector factor*. The latter takes into account the symmetry of MO effects. In our case it is the Faraday effect whose symmetry is described by the unitary antisymmetric tensor of the third rank, known the Levi-Civita tensor, and as a result, the efficiency of the MO interaction δ is described by a mixed product of the three interacting polarizations:[54]

$$\delta=[\vec{e}^{*}_{(s)}\cdot(\vec{m}\times\vec{e}_{(i)})]=[\vec{e}_{(i)}\cdot(\vec{e}_{(s)}\times\vec{m})],$$

where $\vec{e}_{(i)}$ is the polarization of the incident optical wave, $\vec{e}_{(s)}$ is the polarization of the scattered optical wave, and $\vec{m}$ is the polarization of the spin wave. Here we made use of the symmetry of the mixed product with respect to a circular permutation. Besides, in our experiment we used the *p-s* scattering geometry which means, in particular, that the polarization of the *s* type of the scattered wave is normal to the plane of the MO interaction, i.e., the *XZ* plane and consequently $\vec{e}^{*}_{(s)}=\vec{e}_{(s)}$.

The polarization of the incident wave, being of the *p* type, lies in the *XZ* plane. Besides, due to the transversal nature of optical waves, is perpendicular to the wave vector $(\vec{k}\cdot\vec{e}_{(i)})=0$. Hence the non-normalized polarization can be written as

$$\vec{e}_{(i)}=(q+ip)\vec{u}_x-\sin\theta\vec{u}_z.$$

Thus, the polarization of the incident wave is also described by a complex vector. In other words, it is elliptically polarized, which is very important for the following discussion. A second major point consists in the elliptical nature of the polarization of the spin wave. In the Damon-Eshbach geometry, the latter is described by $\vec{u}_x\pm i\omega_H/\omega\vec{u}_z$,[55] where ω is the frequency of the spin wave and $\omega_H=\gamma H$. Sign "+" corresponds to the up-shifted anti-Stokes scattering, while sign "–" corresponds to the downshifted Stokes scattering. In other words, the Stokes line corresponds to scattering by a SW with a positive frequency $-\omega$, while the anti-Stokes one to that by a SW with a negative frequency $+\omega$. Physically, this change in sign amounts to an inversion of the direction of the rotation of the vector of magnetization with the time

reversal, corresponding to the time reversal, which is taken into account mathematically by complex conjugation:

$$\vec{m}^{anti\text{-}Stokes} = \vec{m} = \vec{u}_x + i\frac{\omega_H}{\omega}\vec{u}_z = (\vec{m}^{Stokes})^*.$$

Finally one arrives at two different expressions for the *vector factor* in the scattering efficiency:

$$\delta^{anti\text{-}Stokes} = [\vec{e}_{(i)} \cdot (\vec{e}_{(s)} \times \vec{m})] = \left(\sin\theta - p\frac{\omega_H}{\omega}\right) + iq\frac{\omega_H}{\omega},$$

$$\delta^{Stokes} = [\vec{e}_{(i)} \cdot (\vec{e}_{(s)} \times \vec{m}^*)] = \left(\sin\theta + p\frac{\omega_H}{\omega}\right) + iq\frac{\omega_H}{\omega}.$$

Hence the ratio of the intensities of the Stokes and anti-Stokes lines, describing the Stokes–anti-Stokes asymmetry, mentioned in the text is given by

$$\frac{I^{anti\text{-}Stokes}}{I^{Stokes}} = \frac{\left(\sin\theta - p\frac{\omega_H}{\omega}\right)^2 + \left(q\frac{\omega_H}{\omega}\right)^{-2}}{\left(\sin\theta + p\frac{\omega_H}{\omega}\right)^2 + \left(q\frac{\omega_H}{\omega}\right)^{-2}}. \quad \text{(A1)}$$

[1] A. Fert and L. Piraux, J. Magn. Magn. Mater. **200**, 338 (1999).
[2] J.-E. Wegrowe, T. Wade, X. Hoffer, L. Gravier, J.-M. Bonard, and J.-Ph. Ansermet, Phys. Rev. B **67**, 104418 (2003).
[3] L. Piraux, J. M. George, J. F. Despres, C. Leroy, E. Ferain, R. Legras, K. Ounadjela, and A. Fert, Appl. Phys. Lett. **65**, 2484 (1994).
[4] K. Liu, K. Nagodawithana, P. C. Searson, and C. L. Chien, Phys. Rev. B **51**, 7381 (1995).
[5] S. Dubois, C. Marchal, J. M. Beuken, L. Piraux, J. L. Duvail, A. Fert, J. M. George, and J. L. Maurice, Appl. Phys. Lett. **70**, 396 (1997).
[6] M. Tsoi, J. Z. Sun, M. J. Rooks, R. H. Koch, and S. S. P. Parkin, Phys. Rev. B **69**, 100406(R) (2004).
[7] R. Ferré, K. Ounadjela, J. M. George, L. Piraux, and S. Dubois, Phys. Rev. B **56**, 14066 (1997).
[8] W. Wernsdorfer, B. Doudin, D. Mailly, K. Hasselbach, A. Benoit, J. Meier, J.-Ph. Ansermet, and B. Barbara, Phys. Rev. Lett. **77**, 1873 (1996).
[9] D. Kelly, J.-E. Wegrowe, T.-k. Truong, X. Hoffer, and J.-Ph. Ansermet, Phys. Rev. B **68**, 134425 (2003).
[10] U. Ebels, J.-L. Duvail, P. E. Wigen, L. Piraux, L. D. Buda, and K. Ounadjela, Phys. Rev. B **64**, 144421 (2001).
[11] C. A. Ramos, M. Vasquez, K. Nielsch, K. Pirota, J. Rivas, R. B. Wehrspohn, M. Tovar, R. D. Sanchez, and U. Gosele, J. Magn. Magn. Mater. **272-276**, 1652 (2004).
[12] O. Yalçın, F. Yıldız, M. Özdemir, B. Aktaş, Y. Köseoğlu, M. Bal, and M. T. Tuominen, J. Magn. Magn. Mater. **272-276**, 1684 (2004).
[13] G. Goglio, S. Pignard, A. Radulescu, L. Piraux, I. Huynen, D. Vanhoenacker, and A. Vander Vorst, Appl. Phys. Lett. **75**, 1769 (1999).
[14] M. Demand, A. Encinas-Oropesa, S. Kenane, U. Ebels, I. Huynen, and L. Piraux, J. Magn. Magn. Mater., **249**, 228 (2002).
[15] A. Encinas-Oropesa, M. Demand, L. Piraux, I. Huynen, and U. Ebels, Phys. Rev. B **63**, 104415 (2001).
[16] A. Encinas-Oropesa, M. Demand, L. Piraux, U. Ebels, and I. Huynen, J. Appl. Phys. **89**, 6704 (2001).
[17] T. Jonsson, P. Nordblad, and P. Svedlindh, Phys. Rev. B **57**, 497 (1998).
[18] P. E. Jönsson, S. Felton, P. Svedlindh, P. Nordblad, and M. F. Hansen, Phys. Rev. B **64**, 212402 (2001).
[19] Xi Chen, S. Bedanta, O. Petracic, W. Kleemann, S. Sahoo, S. Cardoso, and P. P. Freitas, Phys. Rev. B **72**, 214436 (2005).
[20] S. Bedanta, T. Eimüller, W. Kleemann, J. Rhensius, F. Stromberg, E. Amaladass, S. Cardoso, and P. P. Freitas, Phys. Rev. Lett. **98**, 176601 (2007).
[21] T. Wolfram and T. E. DeWames, Prog. Surf. Sci. **2**, 233 (1972).
[22] S. M. Cherif, Y. Roussigné, and P. Moch, Phys. Rev. B **59**, 9482 (1999).
[23] R. Arias and D. L. Mills, Phys. Rev. B **63**, 134439 (2001).
[24] R. Arias and D. L. Mills, Phys. Rev. B **67**, 094423 (2003).
[25] E. V. Tartakovskaya, Phys. Rev. B **71**, 180404(R) (2005).
[26] C. Mathieu, J. Jorzick, A. Frank, S. O. Demokritov, A. N. Slavin, B. Hillebrands, B. Bartenlian, C. Chappert, D. Decanini, F. Rousseaux, and E. Cambril, Phys. Rev. Lett. **81**, 3968 (1998).
[27] S. O. Demokritov, B. Hillebrands, and A. N. Slavin, Phys. Rep. **348**, 441 (2001).
[28] G. Gubbiotti, P. Candeloro, L. Businaro, E. Di Fabrizio, A. Gerardino, R. Ziveri, M. Conti, and G. Carlotti, J. Appl. Phys. **93**, 7595 (2003).
[29] Z. K. Wang, M. H. Kuok, S. C. Ng, H. J. Fan, D. J. Lockwood, K. Nielsch, and R. B. Wehrspohn, Mater. Phys. Mech. **4**, 22 (2001).
[30] Z. K. Wang, M. H. Kuok, S. C. Ng, D. J. Lockwood, M. G. Cottam, K. Nielsch, R. B. Wehrspohn, and U. Gôsele, Phys. Rev. Lett. **89**, 027201 (2002).
[31] A. A. Stashkevich, Y. Roussigné, A. I. Stognij, N. N. Novitskii, M. P. Kostylev, G. A. Wurtz, A. V. Zayats, and L. V. Lutsev, Phys. Rev. B **78**, 212404 (2008).
[32] A. A. Stashkevich, Y. Roussigné, A. I. Stognij, N. N. Novitskii, G. A. Wurtz, A. V. Zayats, G. Viau, G. Chaboussant, F. Ott, S. Gautrot, P. Djemia, M. P. Kostylev, L. V. Lutsev, and V. Belotelov, J. Appl. Phys. **104**, 093912 (2008).
[33] Z. K. Wang, H. S. Lim, H. Y. Liu, S. C. Ng, M. H. Kuok, L. L. Tay, D. J. Lockwood, M. G. Cottam, K. L. Hobbs, P. R. Larson, J. C. Keay, G. D. Lian, and M. B. Johnson, Phys. Rev. Lett. **94**, 137208 (2005).
[34] P. Evans, W. R. Hendren, R. Atkinson, G. A. Wurtz, W. Dickson, A. V. Zayats, and R. J. Pollard, Nanotechnology **17**, 5746 (2006).
[35] K. Sato, Jpn. J. Appl. Phys. **20**, 2403 (1981).
[36] E. Tartakovskaya, A. Vovk, and V. Golub, Phys. Status Solidi A **205**, 1787 (2008).
[37] Y. Roussigné, S. M. Cherif, and P. Moch, J. Magn. Magn. Mater. **263**, 289 (2003).

[38] J. A. Osborn, Phys. Rev. **67**, 351 (1945).
[39] K. Yu. Guslienko, S. O. Demokritov, B. Hillebrands, and A. N. Slavin, Phys. Rev. B **66**, 132402 (2002).
[40] M. P. Kostylev, A. A. Stashkevich, N. A. Sergeeva, and Y. Roussigné, J. Magn. Magn. Mater. **278**, 397 (2004).
[41] Y. Roussigné, S. M. Chérif, C. Dugautier, and P. Moch, Phys. Rev. B **63**, 134429 (2001).
[42] A. Aharoni, J. Appl. Phys. **69**, 7762 (1991).
[43] J. Jorzick, S. O. Demokritov, B. Hillebrands, M. Bailleul, C. Fermon, K. Y. Guslienko, A. N. Slavin, D. V. Berkov, and N. L. Gorn, Phys. Rev. Lett. **88**, 047204 (2002).
[44] C. Bayer, S. O. Demokritov, B. Hillebrands, and A. N. Slavin, Appl. Phys. Lett. **82**, 607 (2003).
[45] R. L. Stamps and B. Hillebrands, Phys. Rev. B **44**, 12417 (1991).
[46] B. A. Kalinikos, N. V. Kozhus, M. P. Kostylev, and A. N. Slavin, J. Phys. Condens. Matter **2**, 9861 (1990).
[47] P. Grünberg and F. Metawe, Phys. Rev. Lett. **39**, 1561 (1977).
[48] R. E. Camley and D. L. Mills, Phys. Rev. B **18**, 4821 (1978).
[49] M. G. Cottam, J. Phys. C **12**, 1709 (1979).
[50] R. E. Camley, P. Grünberg, and C. M. Mayr, Phys. Rev. B **26**, 2609 (1982).
[51] http://www.comsol.fr/products/multiphysics/
[52] A. G. Gurevich and G. A. Melkov, *Magnetization Oscillations and Waves* (CRC Press, New York, 1996).
[53] M. Born and E. Wolf, *Principles of Optics* (Pergamon Press, New York, 1964).
[54] A. A. Stashkevich, in *High-Frequency Processes in Magnetic Materials*, edited by G. Srinivasan and A. N. Slavin (World Scientific, Singapore, 1995).
[55] B. A. Kalinikos, in *Linear and Nonlinear Spin Waves in Magnetic Films and Superlattices*, edited by M. G. Cottam (World Scientific, Singapore, 1994), pp. 90–156.